ISSN 1674-1056
http://cpb.iphy.ac.cn
http://iopscience.iop.org/cpb
中国物理 B
Chinese Physics
中国物理
Chinese Physics B

Response features of nonlinear circumferential guided wave on early damage in inner layer of a composite circular tube

Ming-Liang Li(李明亮), Liang-Bing Liu(刘良兵), Guang-Jian Gao(高广健), Ming-Xi Deng(邓明晰), Ning Hu(胡宁), Yan-Xun Xiang(项延训), Wu-Jun Zhu(朱武军)

Citation: Chin. Phys. B . 2019, 28(4): 044301. **doi:** 10.1088/1674-1056/28/4/044301
Journal homepage: http://cpb.iphy.ac.cn; http://iopscience.iop.org/cpb

What follows is a list of articles you may be interested in

Manipulation of acoustic wavefront by transmissive metasurface based on pentamode metamaterials

Ying Liu(刘颖), Yi-Feng Li(李义丰), Xiao-Zhou Liu(刘晓宙)
Chin. Phys. B . 2019, 28(2): 024301. **doi:** 10.1088/1674-1056/28/2/024301

Theoretical prediction of the yield of strong oxides under acoustic cavitation

Jing Sun(孙晶), Zhuangzhi Shen(沈壮志), Runyang Mo(莫润阳)
Chin. Phys. B . 2019, 28(1): 014301. **doi:** 10.1088/1674-1056/28/1/014301

Thermoacoustic-reflected focusing lens based on acoustic Bessel-like beam with phase manipulation

An-Ru Hou(侯安茹), Wen-Ting Gao(高文婷), Jiao Qian(钱姣), Hong-Xiang Sun(孙宏祥), Yong Ge(葛勇), Shou-Qi Yuan(袁寿其), Qiao-Rui Si(司乔瑞), Xiao-Jun Liu(刘晓峻)
Chin. Phys. B . 2018, 27(12): 124301. **doi:** 10.1088/1674-1056/27/12/124301

Bidirectional asymmetric acoustic focusing with two flat acoustic metasurfaces

Di-Chao Chen(陈帝超), Xing-Feng Zhu(朱兴凤), Qi Wei(魏琦), Da-Jian Wu(吴大建)
Chin. Phys. B . 2018, 27(12): 124302. **doi:** 10.1088/1674-1056/27/12/124302

Influence of mode conversions in the skull on transcranial focused ultrasound and temperature fields utilizing the wave field separation method: A numerical study

Xiang-Da Wang(王祥达), Wei-Jun Lin(林伟军), Chang Su(苏畅), Xiu-Ming Wang(王秀明)
Chin. Phys. B . 2018, 27(2): 024302. **doi:** 10.1088/1674-1056/27/2/024302

Response features of nonlinear circumferential guided wave on early damage in inner layer of a composite circular tube*

Ming-Liang Li(李明亮)[1], Liang-Bing Liu(刘良兵)[1], Guang-Jian Gao(高广健)[1], Ming-Xi Deng(邓明晰)[1,†], Ning Hu(胡宁)[1], Yan-Xun Xiang(项延训)[2,‡], and Wu-Jun Zhu(朱武军)[2]

[1] *College of Aerospace Engineering, Chongqing University, Chongqing* 400044, *China*
[2] *School of Mechanical and Power Engineering, East China University of Science and Technology, Shanghai* 200237, *China*

(Received 13 January 2019; revised manuscript received 14 February 2019; published online 5 March 2019)

A theoretical model to analyze the nonlinear circumferential guided wave (CGW) propagation in a composite circular tube (CCT) is established. The response features of nonlinear CGWs to early damage [denoted by variations in third-order elastic constants (TOECs)] in an inner layer of CCT are investigated. On the basis of the modal expansion approach, the second-harmonic field of primary CGW propagation can be assumed to be a linear sum of a series of double-frequency CGW (DFCGW) modes. The quantitative relationship of DFCGW mode versus the relative changes in the inner layer TOECs is then investigated. It is found that the changes in the inner layer TOECs of CCT will obviously affect the driving source of DFCGW mode and its modal expansion coefficient, which is intrinsically able to influence the efficiency of cumulative second-harmonic generation (SHG) by primary CGW propagation. Theoretical analyses and numerical simulations demonstrate that the second harmonic of primary CGW is monotonic and very sensitive to the changes in the inner layer TOECs of CCT, while the linear properties of primary CGW propagation almost remain unchanged. Our results provide a potential application for accurately characterizing the level of early damage in the inner layer of CCT through the efficiency of cumulative SHG by primary CGW propagation.

Keywords: circumferential guided wave (CGW), early damage, inner layer of composite circular tube, second-harmonic generation (SHG)

PACS: 43.35.+*d*, 43.25.+*y*, 43.20.Mv **DOI:** 10.1088/1674-1056/28/4/044301

1. Introduction

Composite circular tubes (CCTs), which are generally composed of two circular layers of different metals,[1,2] are widely served in the petroleum and power plant industries, *etc*.[3,4] However, complicated stress and corrosive environments will inevitably lead to the degradation of and even damage to CCT, where the inner layer is more vulnerable to damage than the outer layer, especially to the mechanical degradation of and even damage to the inner layer material resulting from periodic thermal stress and electrochemical corrosion.[1,2] Considering the safety and reliability of the CCT structure in service, it is of great significance to establish a method of accurately characterizing and assessing the level of early damage in the inner layer material. Based on the fact that the nonlinear ultrasonic techniques are much more sensitive to early damage to material than the linear ultrasonic waves,[5–9] and that the circumferential guided waves (CGWs) travelling along the circumference of a tube have the advantage of evaluating early damage to tube materials,[10] it is necessary to further understand the response features of second-harmonic generation (SHG) by primary CGW propagation to the early damage to the inner layer material of CCT.

Deng *et al.* recently proposed a theoretical model to analyze the nonlinear effect of primary (fundamental) CGW propagation,[10] and then implemented the experimental investigation in a single layer circular tube, where the cumulative second harmonic by primary CGW propagation can be observed for evaluating the material accumulated damage.[11] In addition, the influence of change in the inner layer thickness of CCT on effect of SHG has been analyzed by Li *et al.*[12] Previous research has shown that the macroscopic damage to material and structure can be characterized by the relative changes in the linear acoustic parameters, which are inherently related to the second-order elastic constant (SOEC).[13–15] However, in the early damage level of material, the linear acoustic parameters almost remain unchanged, while the relative acoustic nonlinearity parameter β_{R} shows a remarkable rising tendency with the accumulation of material damage.[13–15] Meanwhile, β_{R} is closely related to the second- and the third-order elastic constants (TOECs).[6,16] An increase in β_{R} should be attributed to the increase in the TOECs of material, while change to the SOECs is inconsiderable in the early damage.[13–16]

Previous investigations of the nonlinear effect of primary CGW propagation have confirmed that the accumulated damage to a single layer circular tube can be quantitatively assessed by β_{R}.[11] It can be expected that the early damage

*Project supported by the National Natural Science Foundation of China (Grant Nos. 11834008, 11474361, 11632004, and 11622430).
†Corresponding author. E-mail: dengmx65@yahoo.com
‡Corresponding author. E-mail: yxxiang@ecust.edu.cn
© 2019 Chinese Physical Society and IOP Publishing Ltd

to the inner layer material (characterized by variation in its TOECs) of CCT may also affect the cumulative second harmonics of primary CGW. Therefore, the present investigation will analyze how the efficiency of cumulative SHG by primary CGW propagation is affected by early damage to the inner layer material of a CCT. Our results exhibit a promising means for accurately evaluating the early damage to inner layer through β_{R} by primary CGW propagation.

2. Theoretical fundamentals

A schematic diagram of the CCT model is shown in Fig. 1, where the materials of the CCT are assumed to be isotropic, homogeneous and dispersionless. It should be noted that the model of the CCT in Fig. 1 is also used for the finite element (FE) analysis, the ends C and C', and also the excitation stress T_{rr} will be described in more detail in Section 4. A CCT with a perfect interface is considered and the mechanical conditions at $r = R_2$ can be given by[17]

$$\begin{aligned} P_{rr(1)} &= P_{rr(2)}, \quad P_{\theta r(1)} = P_{\theta r(2)}, \\ U_{r(1)} &= U_{r(2)}, \quad U_{\theta(1)} = U_{\theta(2)}, \end{aligned} \tag{1}$$

where $U_{r(i)} = \boldsymbol{U}_{(i)} \cdot \hat{\boldsymbol{r}}$ and $U_{\theta(i)} = \boldsymbol{U}_{(i)} \cdot \hat{\boldsymbol{\theta}}$ are the radial and circumferential component of displacement field $\boldsymbol{U}_{(i)}$, the radial and circumferential component of the stress are, respectively, denoted by $P_{rr(i)}$ and $P_{\theta r(i)}$, the subscript number $i = 1$ and 2 in U and P, which correspond to layers 1 (inner layer) and 2 (outer one) in Fig. 1, and $\hat{\boldsymbol{r}}$ and $\hat{\boldsymbol{\theta}}$ are, respectively, the unit radial and circumferential vectors.

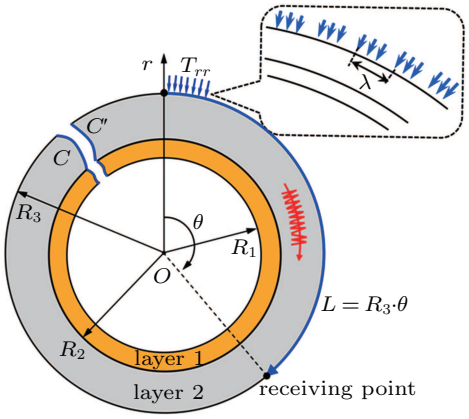


Fig. 1. Schematic diagram of the CCT model used for analyzing CGW propagation.

According to the modal expansion approach for waveguide excitation,[10–12] when the l-th primary CGW mode with angle frequency ω (denoted by $\boldsymbol{U}_{(i)}^{(\omega,l)}$) travels along the circumferential direction as shown in Fig. 1, the linear sum of a series of double-frequency CGW (DFCGW) modes constitutes the acoustic field of the second harmonic (denoted by $\boldsymbol{U}^{(2\omega)}$), namely[10–12]

$$\begin{cases} \boldsymbol{U}^{(2\omega)} = \sum\limits_m a_m(\theta) \boldsymbol{U}^{(2\omega,m)}(r), \\ a_m(\theta) = \dfrac{(F_m^{\mathrm{S}} + F_m^{\mathrm{V}})}{4P_{mm}} \cdot \dfrac{\sin(\Delta n \theta)}{\Delta n} \cdot \exp[\mathrm{j} n^{(2\omega,m)} \theta + \mathrm{j}\Delta n \theta], \end{cases} \tag{2}$$

where $a_m(\theta)$ is the expansion coefficient for the m-th DFCGW mode; $\Delta n = [n^{(\omega,l)} - n^{(2\omega,m)}/2]$ is used to describe the dispersion degree between the l-th primary CGW and the m-th DFCGW; $n^{(\omega,l)}$ and $n^{(2\omega,m)}$ are, respectively, the dimensionless angular wave number of the l-th primary CGW and m-th DFCGW; P_{mm} is the average power flow of the m-th DFCGW mode (per unit width perpendicular to the tube section), *i.e.*[10–12]

$$P_{mm} = \mathrm{Re} \sum_{i=1}^{2} \int_{\mathrm{R_i}}^{R_{i+1}} \left\{ -\frac{\mathrm{j}\omega}{r} \left[\tilde{U}_{(i)}^{(2\omega,m)}(r) \times \boldsymbol{P}_{(i)}^{(2\omega,m)}(r) \right] \right\} \cdot \hat{\boldsymbol{\theta}} \mathrm{d}r, \tag{3}$$

where $\boldsymbol{U}_{(i)}^{(2\omega,m)}(r)$ and $\boldsymbol{P}_{(i)}^{(2\omega,m)}(r)$ are, respectively, the corresponding displacement field function and stress tensor in the i-th layer ($i = 1, 2$); the sign '$\sim$' in Eq. (3) means that the complex conjugate is taken for the corresponding physical variables; R_j ($j = 1$, 2, or 3) represents the radius of the CCT. The surface and bulk driving sources (F_m^{S} and F_m^{V}) are, respectively, expressed as[10–12]

$$F_m^{\mathrm{S}} = 2\mathrm{j}\omega \sum_{i=1}^{2} \left\{ \tilde{U}_{(i)}^{(2\omega,m)}(r) \cdot \boldsymbol{P}[\boldsymbol{U}_{(i)}^{(\omega,l)}] \right\} \cdot \hat{\boldsymbol{r}} \Big|_{r=R_i}^{r=R_{i+1}}, \tag{4}$$

and

$$F_m^{\mathrm{V}} = 2\mathrm{j}\omega \sum_{i=1}^{2} \int_{\mathrm{R_i}}^{R_{i+1}} \left\{ \tilde{U}_{(i)}^{(2\omega,m)}(r) \cdot \boldsymbol{F}[\boldsymbol{U}_{(i)}^{(\omega,l)}] \right\} \mathrm{d}r, \tag{5}$$

which are dependent on the second-order traction stress tensor $\boldsymbol{P}[\boldsymbol{U}_{(i)}^{(\omega,l)}]$ and the second-order bulk driving force $\boldsymbol{F}[\boldsymbol{U}_{(i)}^{(\omega,l)}]$. The $\boldsymbol{P}[\boldsymbol{U}_{(i)}^{(\omega,l)}]$ is the nonlinear term in the expression of the first Piola–Kirchhoff stress tensor, and $\boldsymbol{F}[\boldsymbol{U}_{(i)}^{(\omega,l)}]$ is determined by $\boldsymbol{F}[\boldsymbol{U}_{(i)}^{(\omega,l)}] = \nabla \cdot \boldsymbol{P}[\boldsymbol{U}_{(i)}^{(\omega,l)}]$. Both $\boldsymbol{F}[\boldsymbol{U}_{(i)}^{(\omega,l)}]$ and $\boldsymbol{P}[\boldsymbol{U}_{(i)}^{(\omega,l)}]$ can be found in Refs. [10] and [11].

When the phase velocity of the l-th primary CGW mode matches with that of the m-th DFCGW (*i.e.*, $\Delta n = 0$, or $\Delta n \approx 0$), the second-harmonic field $\boldsymbol{U}^{(2\omega)}$ generated by the l-th primary CGW mode propagation mainly depends on the m-th DFCGW mode, and the contribution of other DFCGW modes to the second-harmonic field is negligible.[10–12] Thus, equation (2) can be written as

$$\boldsymbol{U}^{(2\omega)} = \frac{(F_m^{\mathrm{S}} + F_m^{\mathrm{V}})}{4P_{mm}} \cdot \boldsymbol{U}^{(2\omega,m)}(r) \cdot \theta \cdot \exp[\mathrm{j} n^{(2\omega,m)} \theta]. \tag{6}$$

To effectively investigate the influence of early damage to the inner layer material on the efficiency of cumulative SHG, a special mode pair which satisfies the phase velocity matching is selected.[6,10,16] The physical quantities, such as $\boldsymbol{U}_{(i)}^{(\omega,l)}$, $\boldsymbol{U}_{(i)}^{(2\omega,m)}$, and P_{mm} are dependent on mass density $\rho_{(i)}$, radius R_j and SOECs, while the other quantities, such as $\boldsymbol{P}[\boldsymbol{U}_{(i)}^{(\omega,l)}]$,

$\boldsymbol{F}[\boldsymbol{U}_{(i)}^{(\omega,l)}]$, F_m^{S} and F_m^{V} are dependent on mass density $\rho_{(i)}$, radius R_j, SOECs and TOECs, *i.e.*[10–12]

$$\boldsymbol{U}_{(i)}^{(\omega,l)},\ \boldsymbol{U}_{(i)}^{(2\omega,m)} \text{ and } P_{mm} = \text{Function}[\text{SOECs}, R_j, \rho_{(i)}], \quad (7)$$

$$\boldsymbol{P}[\boldsymbol{U}_{(i)}^{(\omega,l)}],\ \boldsymbol{F}[\boldsymbol{U}_{(i)}^{(\omega,l)}],\ F_m^{\mathrm{S}} \text{ and } F_m^{\mathrm{V}} = \text{Function}[\text{SOECs}, \text{TOECs}, R_j, \rho_{(i)}]. \quad (8)$$

There is a considerable change in the elastic nonlinearity (described by the TOECs, *i.e.*, A, B, and C) even if the elastic linearity of material (described by the SOECs, *i.e.*, λ and μ) has no or inconsiderable change in the early stage of material damage.[15,16] This will lead to changes of $a_m(\theta)$ in Eq. (2). Generally, the ratio A_2/A_1^2 (*i.e.*, the relative acoustic nonlinearity parameter β_{R}) can directly be used to evaluate the material damage,[13–16] where A_1 and A_2 are, respectively, the amplitude of the primary wave $\boldsymbol{U}^{(\omega,l)} \cdot \hat{\theta}$ and the double-frequency mode $a_m(\theta)\boldsymbol{U}^{(2\omega,m)}(r) \cdot \hat{\theta}$ at the outer surface $r = R_3$. Thus, β_{R} may show a remarkable response to the accumulation of material damage since A_2 increases with the increase in the TOECs of the material.[11,15,16]

These analyses indicate that the second-harmonic field $\boldsymbol{U}^{(2\omega)}$ is inherently related to the TOECs and SOECs of material, while the linear acoustic parameters (*e.g.*, A_1 or $n^{(\omega,l)}$) are only associated with the SOECs and remain unchanged in the early damage stage of materials. Consequently, the early damage to the inner layer of the CCT may be quantitatively evaluated by the efficiency of cumulative SHG by primary CGW propagation, specifically, by using β_{R} as measured with second harmonics generated.

3. Numerical analyses

The materials of the CCT (see Fig. 1) from the inner layer to the outer layer are, respectively, considered to be copper and steel, and their radii are set to be $R_1 = 103.5$ mm, $R_2 = 104.5$ mm, and $R_3 = 107.5$ mm. The material parameters of the CCT in Fig. 1 are given in Table 1.

Table 1. Material parameters of CCT.[18]

Material	Mass density ρ/(kg/m^3)	Longitudinal wave velocity c_{L}/(km/s)	Shear wave velocity c_{T}/(km/s)	TOECs (GPa)		
				A	B	C
Copper	8980	4.390	2.140	–1480	150	–320
Steel	7900	5.640	3.070	–720	–230	180

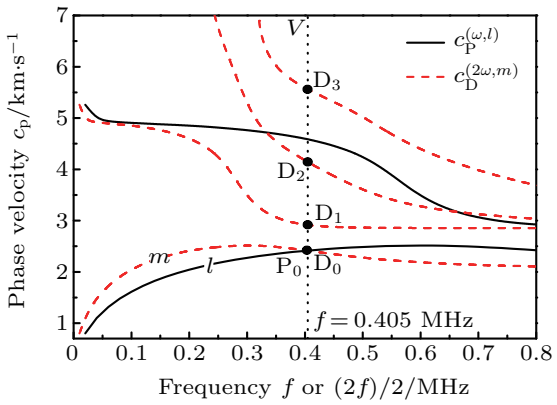


Fig. 2. Dispersion curves of CGWs in the CCT with a perfect interface.

Figure 2 shows the phase velocity dispersion curves of the primary CGW and DFCGWs. The intersections between the dotted line V and the DFCGW dispersion curves denote the DFCGW modes constituting the field of the second harmonics by the l-th primary CGW mode (point P_0 in Fig. 2) at the driving frequency $f = 0.405$ MHz. The phase velocity matching ($c_{\mathrm{P}_0}^{(\omega,l)} = c_{\mathrm{D}_0}^{(2\omega,m)} = 2.415$ km/s) is satisfied at points P_0 and D_0 in Fig. 2. Therefore, the m-th DFCGW mode (point D_0) may have a cumulative growth effect, and the contribution of other DFCGW modes (denoted by points D_1, D_2, and D_3, *etc.*) to the second-harmonic field is negligible due to the mismatching of their phase velocities with $c_{\mathrm{P}_0}^{(\omega,l)}$.[10–12,19,20] Figure 3 shows the curves of displacement amplitudes of the DFCGW modes at $r = R_3$ versus circumferential angle θ, where A_1 is the amplitude of the l-th primary CGW. Since the phase velocity matching condition $c_{\mathrm{P}_0}^{(\omega,l)} = c_{\mathrm{D}_0}^{(2\omega,m)}$ is satisfied at the driving frequency $f = 0.405$ MHz, the m-th DFCGW mode (point D_0) grows linearly with the increasing circumferential angle θ.

Accordingly, the l-th primary CGW mode (point P_0) and the m-th DFCGW mode (point D_0) at the driving frequency $f = 0.405$ MHz (denoted by the line V in Fig. 2) are the mode pair desired for the next analyses.

In the early-damage stage, where changes in the SOECs of material are inconsiderable, variation in β_{R} relative to its initial value should be mainly attributed to the changes in the TOECs of material. To highlight the investigation of assessing early damage to the inner layer (characterized by changes in the TOECs) by using β_{R}, for simplicity, the TOECs of the inner layer material are assumed to change from its initial values (A, B, C) to (eA, eB, eC), through which the degradation of and damage to the inner layer can be conveniently described by only using one parameter (*i.e.*, the scale coefficient e), while the remaining material properties and geometric parameters (R_i) of the CCT are kept unchanged in the analysis process. According to Eq. (8), for the mode pair selected in Fig. 2 (de-

noted by points P_0 and D_0), the corresponding parameters and expansion coefficients of the m-th DFCGW mode (point D_0) are calculated and given in Table 2, where some values of typical scale coefficient e vary from 1.00 to 1.60 in steps of 0.10 (*i.e.*, $\Delta e = 0.10$).

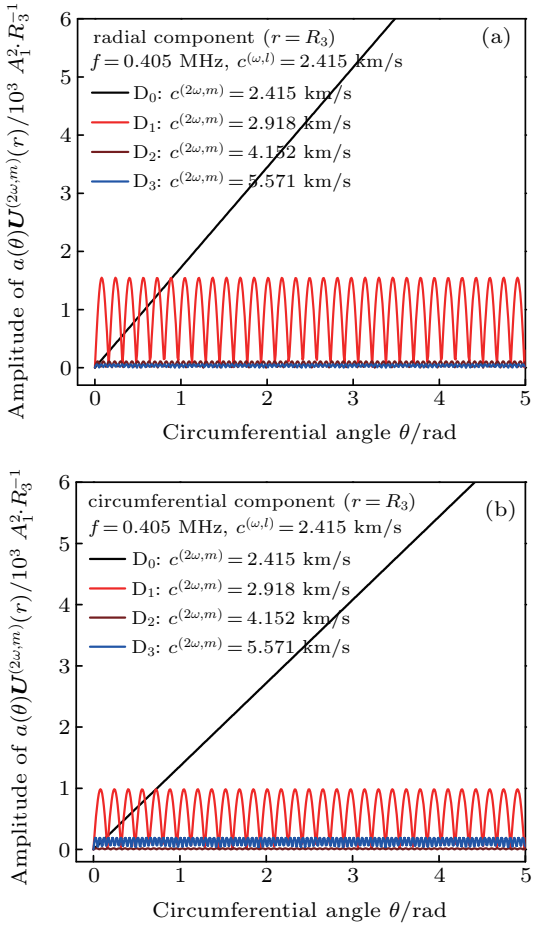


Fig. 3. Displacement amplitudes of some DFCGW modes on outer surface of CCT: (a) radial component, (b) circumferential component.

Table 2. Corresponding parameters and expansion coefficients of m-th DFCGW mode with different values of e ($\theta = 2.14$).

e	$\left\lvert \frac{(F_m^{\mathrm{S}} + F_m^{\mathrm{V}}) \cdot R_3}{4P_{mm} \cdot U^{(\omega,l)}\lvert_{r=R_3}} \right\rvert \times 10^{-3}$/arb. units	$a_m(\theta)$/arb. units
1.00	5.06	(1.78, 1.70)
1.10	5.32	(1.87, 1.79)
1.20	5.59	(1.97, 1.88)
1.30	5.86	(2.06, 1.97)
1.40	6.13	(2.15, 2.06)
1.50	6.39	(2.25, 2.15)
1.60	6.66	(2.34, 2.24)

According to Table 2, the curve of normalized amplitude of $a_m(\theta)\boldsymbol{U}^{(2\omega,m)}(r) \cdot R_3/A_1^2$ versus scale coefficient e of the inner layer TOECs is shown in Fig. 4 (at $\theta = 2.14$). Obviously, the amplitude of $a_m(\theta)\boldsymbol{U}^{(2\omega,m)}(r) \cdot R_3/A_1^2$ grows linearly with scale coefficient e increasing. The numerical results demonstrate that the cumulative second harmonic can monotonically and sensitively reflect changes in the inner layer's TOECs of the CCT.

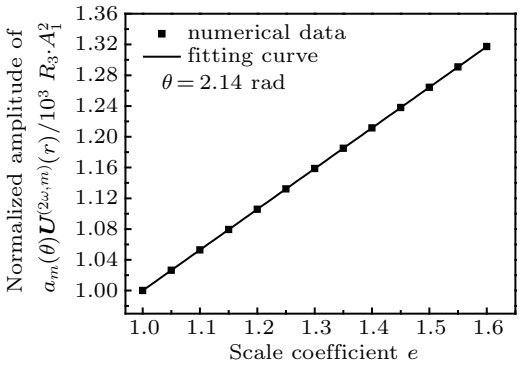


Fig. 4. Normalized amplitude of $a_m(\theta)\boldsymbol{U}^{(2\omega,m)}(r) \cdot R_3/A_1^2$ *versus* e ($\Delta e = 0.05$) at circumferential angle $\theta = 2.14$ rad.

4. Finite element simulations

The response features of cumulative second harmonics in the CCT with different TOECs of the inner layer will be performed with an FE software ABAQUS®, which can avoid the experimental complexity.[21] The model of FE simulation is also shown in Fig. 1. It should be noticed that the FE simulation of nonlinear CGW propagation in ABAQUS is set up according to Cartesian coordinate system, while the Polar coordinate system is adopted for the theoretical model. Consequently, for further analyses, the FE simulation results obtained in the Cartesian coordinate system will be converted into those in the Polar coordinate system.

The excitation stress T_{rr}, which is applied to the outer surface of the CCT in Fig. 1, can simultaneously generate the CGW modes propagating clockwise and counterclockwise along the circumference. In the FE simulation, we only take the CGWs propagating clockwise into account. Consequently, the CCT is cut off at the ends C and C' (see Fig. 1) to avoid the interference of CGW propagating counterclockwise. Meanwhile, the reflected waves by the said ends are weakened through taking the technique of infinite element meshes CINPE4.[22] The nonlinear stress-strain constitutive relations are introduced into the simulation model through invoking a user-defined material subroutine VUMAT.[21,22] To effectively generate the pure primary CGW mode desired (point P_0 in Fig. 2) and inhibit the unwanted CGW modes, the excitation stress T_{rr} with a special spatial distribution λ is applied to the outer surface of the CCT (shown in Fig. 1), where λ is the wavelength of the primary P_0 CGW mode desired (about 5.970 mm) and the arc length of T_{rr} is 5λ. The signal of the excitation stress T_{rr} (only with the radial component) is a 20-cycle Hanning windowed sinusoidal tone burst at a driving frequency f of 0.405 MHz (given by the dotted line V in Fig. 2), whose magnitude is set to 15 MPa.

The geometrical and material parameters of the CCT for FE simulations are the same as those given in Section 3. For

the undamaged CCT (*i.e.*, $e = 1.00$) in Fig. 1, the temporal signals of the circumferential stress component of primary CGWs are shown in Fig. 5, where the receiving points are, respectively, located at the arc length $L_1 = 230.8$ mm and $L_2 = 292.1$ mm away from the source T_{rr}. The theoretical group delay time of the primary CGW mode desired is calculated to be $(L_2 - L_1)/c_g^{(\omega,l)} = 21.14$ μs ($c_g^{(\omega,l)}$-group velocity), which is very close to the group delay time 20.70 μs in Fig. 5 (Relative error (RE) is 2.07%). We are thus convinced that the carrier of the wave package shown in Fig. 5 is certainly of the primary CGW mode desired (point P_0 in Fig. 2).

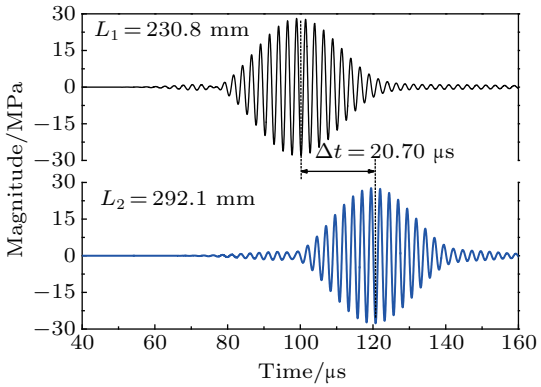


Fig. 5. Time-domain signals of primary CGWs at arc length (a) $L_1 = 230.8$ mm and (b) $L_2 = 292.1$ mm.

For the case where the changes in the inner layer TOECs (denoted by the scale coefficient e from 1.00 to 1.60) take place, the signals similar to that shown in Fig. 5 are simulated and obtained with ABAQUS. To directly observe the temporal response of SHG by the primary CGW, a band-pass (0.7 MHz–0.9 MHz) digital filtering processing is exerted on the time-domain signal, and then the corresponding second-harmonic signal is obtained. Figure 6 shows some typical temporal responses of second harmonics extracted from the time-domain signal (such as that in Fig. 5) with the scale coefficients $e = 1.00$, 1.20, 1.40, and 1.60, where the receiving points are kept unchanged at $\theta = 2.15$ rad. Clearly, the magnitudes of second harmonics grow obviously with the increase in the inner layer TOECs of the CCT.

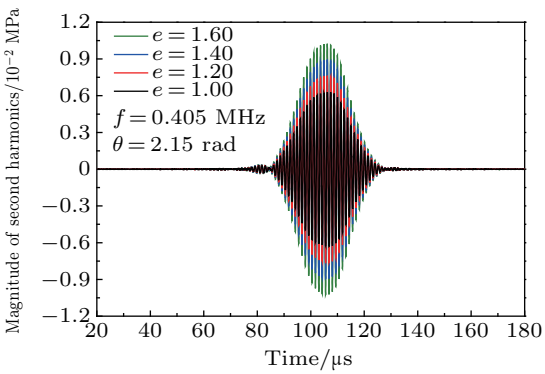


Fig. 6. Time-domain signals of second harmonics at the driving frequency $f = 0.405$ MHz with different values of scale coefficient e.

Then, the fast Fourier transform (FFT) is implemented on the time-domain signals to obtain the fundamental and second harmonic signal. The amplitude–frequency curves of the receiving signals with the values of scale coefficient $e = 1.00$, 1.30, and 1.60 at $\theta = 2.15$ rad are presented in Fig. 7, where the corresponding fundamental-frequency ($f = 0.405$ MHz) and second-harmonic ($f = 0.810$ MHz) amplitudes, denoted by A_1 and A_2, can directly be determined. Clearly, there is an obvious second-harmonic signal at a fundamental frequency of 0.405 MHz with different values of scale coefficient e. It should be noted that within a second-order perturbation, A_2 is far less than A_1.

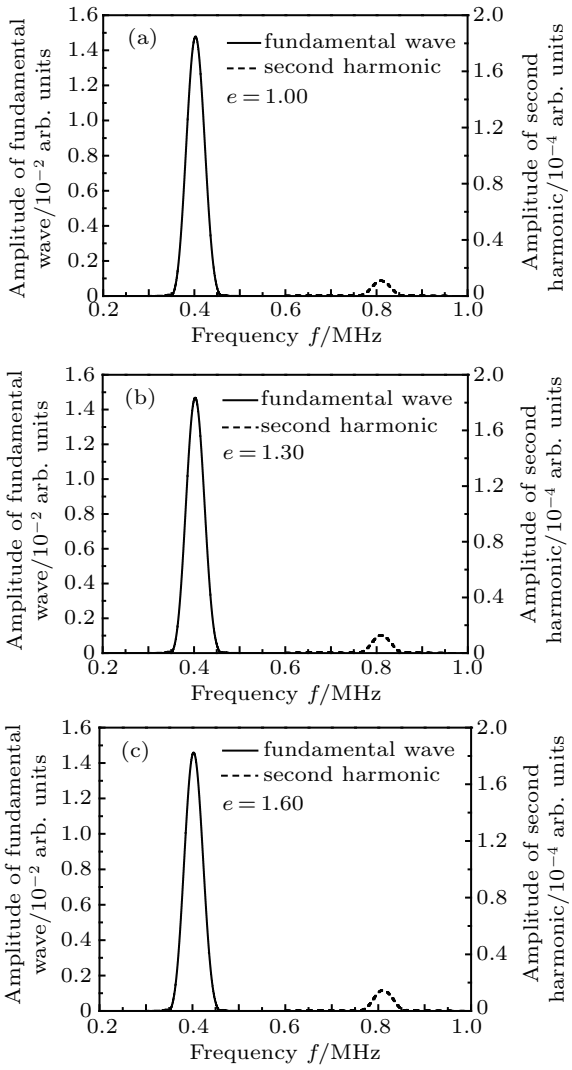


Fig. 7. Amplitude–frequency curves of the fundamental wave and second harmonic for different values of scale coefficient: (a) $e = 1.0$, (b) $e = 1.3$, (c) $e = 1.6$.

According to the amplitude–frequency curves in Fig. 7, the amplitudes of A_1 and A_2, and also the relative acoustic nonlinearity parameter β_R for different values of scale coefficient e can readily be obtained. Figure 8 shows that the normalized value of β_R grows linearly with the increase of scale coefficient e, while the amplitude of fundamental wave A_1 is almost kept unchanged. Clearly, the results of both the numerical analyses in Fig. 4 and the FE simulations in Fig. 8

are consistent, demonstrating that the cumulative second harmonic can monotonically and sensitively reflect changes in the inner layer TOECs of the CCT.

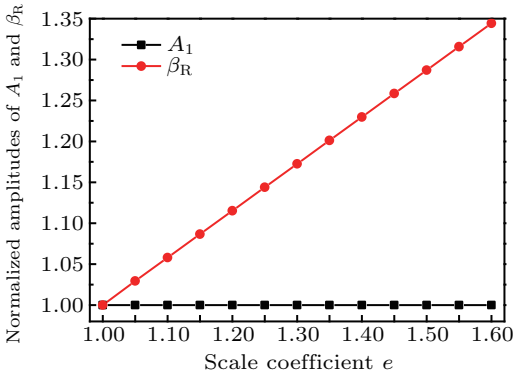


Fig. 8. Curves of normalized A_1 and β_R *versus* scale coefficient e.

5. Conclusions

In this work, we investigate the response features of second harmonics by primary CGW propagation to the early damage to inner layer material (characterized by the changes in the TOECs) of the CCT through the analytical analyses and FE simulations. The deduced analytical expressions indicate that the second-order traction stress tensors and bulk driving forces are inherently related to the SOECs and TOECs of the material, which are the excitation sources to generate a series of DFCGW modes. Consequently, the efficiency of SHG generated by primary CGW propagation can be used to accurately evaluate the early damage to the inner layer. The FE simulations conducted here reveal the complicated physical process of SHG of primary CGW in the CCT with the change in the inner layer TOECs unavailable previously. Both the numerical analyses and FE simulations indicate that the second harmonics of primary CGW can monotonically and sensitively reflect the early damage to the inner layer of the CCT (characterized by changes in the TOECs), while the linear property of primary CGW remains almost unchanged. Our results show a promising means of using the efficiency of cumulative SHG of primary CGW to characterize the early damage level to the inner layer of the CCT structure.

References

[1] Serikov O 2005 *Metallurgist* **49** 347
[2] Torbatia A M, Mirandab R M, Quintino L, Williams S and Yapp D 2011 *J. Mater. Process. Tech.* **211** 1112
[3] Wang H, Han J and Hui Z 2013 *Appl. Mech. Mater.* **278** 487
[4] Zeng D, Deng K, Shi T and Lin Y 2014 *J. Press. Vessel Tech.* **136** 061402
[5] Jhang K Y and Kim K 1999 *Ultrasonics* **37** 39
[6] Kim J, Jacobs L, Qu J and Littles J 2006 *J. Acoust. Soc. Am.* **120** 1266
[7] Deng M X and Pei J F 2007 *Appl. Phys. Lett.* **90** 121902
[8] Deng M X and Xiang Y X 2010 *Chin. Phys. B* **19** 114302
[9] Xiang Y X, Zhu W J, Deng M X and Xuan F Z 2016 *Chin. Phys. B* **25** 024303
[10] Gao G J, Deng M X and Li M L 2015 *Acta. Phys. Sin.* **64** 184303 (in Chinese)
[11] Deng M X, Gao G J, Li M L and Xiang Y X 2017 *Ultrasonics* **75** 209
[12] Li M L, Deng M X, Gao G J, Chen H and Xiang Y X 2017 *Chin. Phys. Lett.* **34** 064302
[13] Hughes D and Kelly J 1953 *Phys. Rev.* **92** 1145
[14] Hikata A, Chick B and Elbaum C 1965 *J. Appl. Phys.* **36** 229
[15] Nagy P B 1998 *Ultrasonics* **36** 375
[16] Hamilton M F and Blackstock D T 1998 *Nonlinear Acoustics* (New York: Academic)
[17] Rokhlin S and Wang Y 1991 *J. Acoust. Soc. Am.* **89** 503
[18] Hearmon R 1979 *Numerical Data and Functional Relationship in Science and Technology Group III* (Berlin: Springer)
[19] Lima W and Hamilton M 2003 *J. Sound Vib.* **265** 819
[20] Deng M X 2003 *J. Appl. Phys.* **94** 4152
[21] Zhu W J, Deng M X, Xiang Y X, Xuan F Z and Liu C J 2016 *Ultrasonics* **68** 134
[22] Simulia Abaqus 6.14 Documentation. http://wufengyun.com:888/v6.14/books/usi/default.htm (2018-04-28)